SCIENCE CHINA
Technological Sciences

Special Topic: Robotics and Intelligent Manufacturing
•Article•

July 2023 Vol.66 No.7: 1869–1882
https://doi.org/10.1007/s11431-022-2369-0

Dynamic modeling and analysis of the 3-PRS power head based on the screw theory and rigid multipoint constraints

MA YiWei[1,2*], TIAN YanLing[1], LIU XianPing[1] & LU ChengHao[2]

[1] *School of Engineering, The University of Warwick, Coventry CV4 7AL, UK;*
[2] *School of Mechanical Engineering, Tianjin University, Tianjin 300072, China*

Received November 30, 2022; accepted March 2, 2023; published online June 8, 2023

This study presents a dynamic modeling and analysis methodology for the 3-PRS parallel mechanism. First, an improved reduced dynamic model of component substructures is proposed using the dynamic condensation technique and the rigid multipoint constraints at the joint/interface level, leading to a minimum set of generalized coordinates for external nodes. Next, the mapping between interface constraint stiffness and global stiffness is illustrated, resulting in an analytical stiffness model of joint substructures. Subsequently, the derived component and joint substructures are synthesized into the entire mechanism based on the Lagrange equation. Finally, a case study illustrates that the lower-order dynamic performances predicted within the proposed approach have the same trend as those obtained from a complete-order finite element model. The root mean square discrepancy of the lower-order natural frequencies between the two models is less than 5.92%, indicating the accuracy and effectiveness of the proposed model. The developed approach can highly and efficiently predict the dynamic performance distributions across the entire workspace and guide the optimal functional design under the virtual machine framework.

dynamic modeling, parallel kinematic machines, screw theory, substructure synthesis, rigid multipoint constraints

Citation: Ma Y W, Tian Y L, Liu X P, et al. Dynamic modeling and analysis of the 3-PRS power head based on the screw theory and rigid multipoint constraints. Sci China Tech Sci, 2023, 66: 1869–1882, https://doi.org/10.1007/s11431-022-2369-0

1 Introduction

As one of the most significant performance parameters of a parallel kinematic machine (PKM), dynamic characteristics represent the capability of the end-reference point to withstand elastic deformations under dynamic cutting loads resulting from the tool-workpiece interaction [1–3]. Due to the position-dependency nature of the PKM dynamics, a reduced semi-analytical model is essential for predicting the lower-order dynamic characteristics and illustrating the strategies for the optimization design [4–6].

The available methods for the dynamic modeling of PKMs are roughly categorized into five categories: lumped parameter method (LPM) [7–9], matrix structural analysis (MSA) [10–13], finite element analysis (FEA) [14–16], transfer matrix method for multibody systems (MSTMM) [17–21], and component mode synthesis (CMS) [22–26]. The components in the LMP and MSA are treated as lumped mass-springs and equivalent spatial beam elements, respectively. The LMP is adapted for the dynamic modeling of PKMs in which the inertial and elastic parameters can be significantly separated. Meanwhile, the MSA is suitable for dynamic systems with slender link structures. Despite the fact that the analytical expressions of stiffness and mass can be directly derived via the LPM and MSA, guaranteeing the calculation accuracy is challenging due to an over-simplified model. To improve the calculation accuracy, the FEA provides a precise description of the deformation field of complex geometrical components and the contact elasticity of joints in the FE software. However, this method is typically

*Corresponding author (email: yi-wei.ma@warwick.ac.uk)

available for model verification or final design prediction considering the re-meshing operations for different configurations.

The MSTMM was proposed by Rui et al. [17–19] to overcome the time-consuming shortcomings of the FEA method. It is an improvement over the traditional transfer matrix method (TMM). The MSTMM is straightforward since the complicated global equation of motion is replaced by deriving the transfer equations and matrices of the overall dynamic system with sufficient modeling flexibility and low-order matrices. Employing this method, Chen et al. [20] derived a dynamic model and state-space representation of the Stewart mechanism considering a rigid moving platform and flexible limbs. Nevertheless, obtaining an accurate reduced model of subsystems in the PKMs, especially for complex geometrical components, is a fundamental challenge for the MSTMM. The CMS organically combines elasticity and structural mechanics, employing static or dynamic condensation to reduce the full FE model of complex geometrical components in the PKMs while keeping the kineto-static or lower-order modes almost unchanged [22,23]. Wu et al. [25] presented a general approach for the stiffness distributions of the parallel mechanism and verified its performance with the FEA results over a reference plane. This approach was employed to predict the lower-order dynamics of a type of 5-degrees-of-freedom (DOF) hybrid mechanism with a minimum group of coordinates [26]. The component substructures were synthesized according to the interface deformation compatibility condition. A challenge of this process is the representation of external nodal DOFs by the condensation node DOFs solved by two common approaches, that is, interpolation and rigid multipoint constraints (RMPC) [27]. Selecting a suitable multipoint constraint equation following the modeler's tendency is a significant problem. In addition, the mapping between each joint and its interfaces, which was ignored in the abovementioned research, must be constructed.

As a typical lower-mobility parallel mechanism, the 3-PRS power head is widely used in multiple industrial areas, including aerospace, automobiles, and shipping, because of its high pose-ability, highly symmetrical kinematics, and high axial stiffness. In contrast to other parallel mechanisms with slender link structures (e.g., Stewart platform and Tricept robot), the components in the actuated limbs of the 3-PRS parallel mechanism are more complex and more challenging to be equivalent. This study introduces an improved reduced dynamic model for this mechanism to provide sufficient guidance for the optimization design under the virtual machine framework. The contributions of this study lie in providing an accurate and practical approach for the lower-order dynamic modeling and analysis of PKMs by combing the screw theory, RMPC, and CMS methods.

2 System description

Figure 1 illustrates the computer-aided design (CAD) model of the 3-PRS parallel mechanism under investigation, which essentially comprises three identical PRS limbs, a moving platform, and a base. In the figure, the R, S, and underlined P denote the passive revolute, spherical, and actuated prismatic joints, respectively. We set the number of the three parallel PRS limbs as 1, 2, and 3 to describe each limb component and joint.

Figures 2 and 3 illustrate the schematic diagram and the reference frames, respectively, of the 3-PRS power head, where $\Delta A_1A_2A_3$ and $\Delta B_1B_2B_3$ are both equilateral triangles. A fixed frame $\mathcal{K}_0$ is placed at the center point A of $\Delta A_1A_2A_3$ with its x and z axes along $\overline{A_3A_2}$ and normal to $\Delta A_1A_2A_3$, respectively. The global reference frame $\mathcal{K}'$ is attached to the end-reference point C of the spindle, with its u and w axes along $\overline{B_3B_2}$ and normal to $\Delta B_1B_2B_3$, respectively. $O_{1,i}$

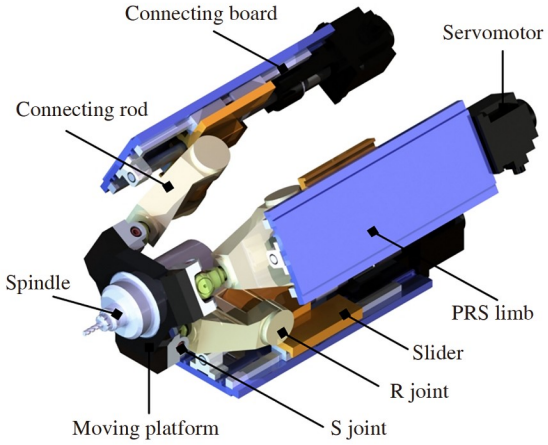

Figure 1 (Color online) CAD model of the 3-PRS parallel mechanism.

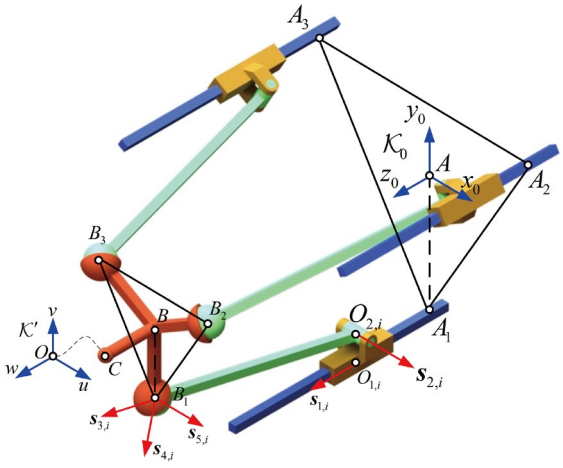

Figure 2 (Color online) Schematic diagram of the 3-PRS parallel mechanism.

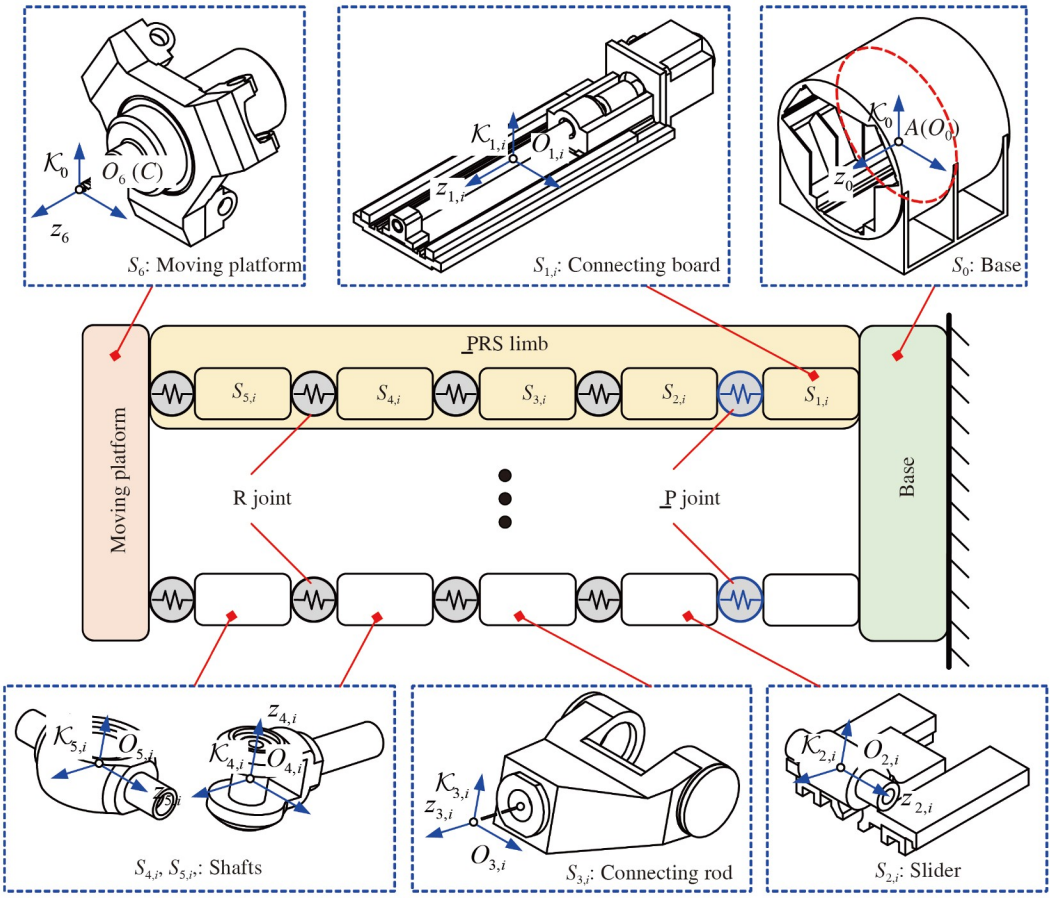

Figure 3 (Color online) Elastic model and body-fixed reference frames of the 3-PRS power head.

(i=1,2,3) denotes the center points of the linear guidance slider system in the P joint. $O_{2,i}$ and $B\left(O_{j,i}, j=3,4,5\right)$ are the center points of the revolute and spherical joints, respectively. The body-fixed frames in limb i, $\mathcal{K}_{j,i}$(j=1,2,3,4,5), are located at $O_{j,i}$ with $z_{j,i}$ along the translational or rotational motion. The unit vectors of each joint in Figure 2 conform to the following relationships:

$$\begin{aligned}&\mathbf{s}_{1,i} \perp \mathbf{s}_{2,i}, \mathbf{s}_{2,i} \perp \mathbf{s}_{3,i},\\ &\mathbf{s}_{3,i} \perp \mathbf{s}_{4,i}, \mathbf{s}_{4,i} \perp \mathbf{s}_{5,i}, i=1,2,3.\end{aligned} \tag{1}$$

The abovementioned reference frames and unit vectors are obtained using the inverse kinematic analysis of the 3-PRS power head when given an end-reference point C configuration [28,29]. Assume that the connecting board in each limb is fixed on the base component.

3 Dynamic modeling

Based on the rigid multipoint constraints and screw theory, this section concentrates on formulating an improved reduced dynamic model of the 3-PRS power head that enables the lower-order dynamic analysis to be accurately and efficiently predicted.

3.1 Improved reduction model of the component substructures

A semi-analytical reduced dynamic model of component substructures is developed in this section. Considering the connecting board as the component substructure i, the local reference frame $\mathcal{K}_{i+1}$ is placed at the center of the joint $i+1$ (prismatic joint) (Figure 4). Without considering the number of the component substructure and the limb number, its undamped equation of motion evaluated in the frame $\mathcal{K}_{i+1}$ is obtained as follows using the CMS method from its full FE model [30,31]:

$$\begin{aligned}&\mathbf{m}\ddot{\mathbf{u}}+\mathbf{k}\mathbf{u}=\mathbf{f},\\ &\mathbf{u}=\left(\mathbf{u}_{\mathrm{E}}^{\mathrm{T}} \quad \mathbf{u}_{\mathrm{P}}^{\mathrm{T}}\right)^{\mathrm{T}}, \mathbf{f}=\left(\mathbf{f}_{\mathrm{E}}^{\mathrm{T}} \quad \mathbf{f}_{\mathrm{P}}^{\mathrm{T}}\right)^{\mathrm{T}},\\ &\mathbf{m}=\begin{bmatrix}\mathbf{m}_{\mathrm{EE}} & \mathbf{m}_{\mathrm{EP}}\\ \mathbf{m}_{\mathrm{PE}} & \mathbf{m}_{\mathrm{PP}}\end{bmatrix}, \mathbf{k}=\begin{bmatrix}\mathbf{k}_{\mathrm{EE}} & \mathbf{k}_{\mathrm{EP}}\\ \mathbf{k}_{\mathrm{PE}} & \mathbf{k}_{\mathrm{PP}}\end{bmatrix},\end{aligned} \tag{2}$$

where $\mathbf{k}$ and $\mathbf{m}$ are the stiffness and mass matrices, respectively, of the component substructure. $\mathbf{f}$ and $\mathbf{u}$ denote the

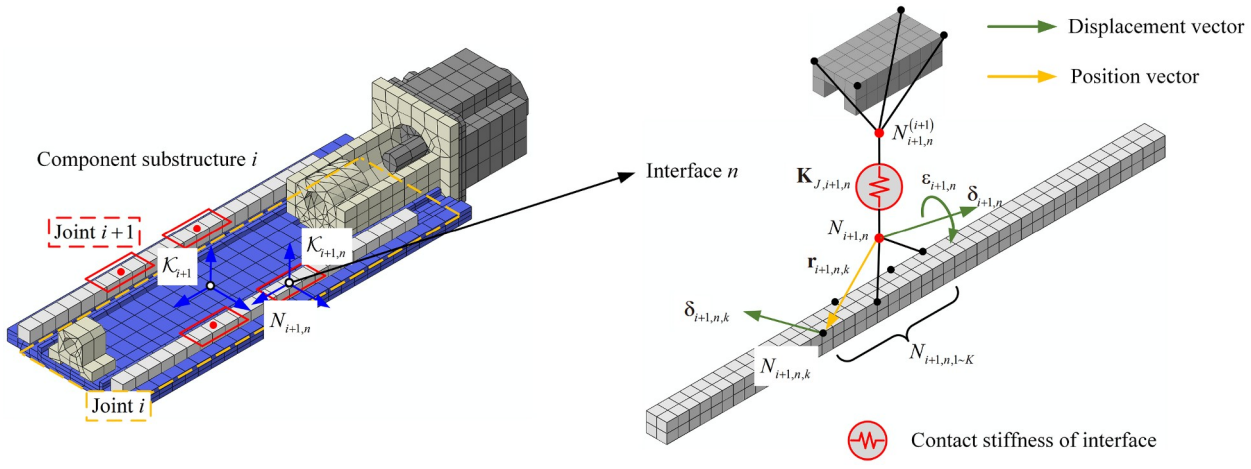

Figure 4 (Color online) Schematic diagram of component substructure i (Connecting board).

force and nodal displacement vectors, respectively, of the component substructure. $\mathbf{u}_{\mathrm{E}}$ and $\mathbf{u}_{\mathrm{P}}$ represent the nodal displacement vectors for the group of external nodes and modal coordinates of the first P-order elastic mode with all external nodes constrained, respectively. The natural frequency of the Pth internal elastic mode is determined as 1.5 to 2 times the maximum excitation frequency of the mechanical system to balance the calculation efficiency and accuracy. Please refer to ref. [32] for more guidance regarding dynamic condensation. $\mathbf{u}_{\mathrm{E}}$ is expressed as follows:

$$\begin{aligned}&\mathbf{u}_{\mathrm{E}}=\begin{pmatrix}\mathbf{u}_i^{\mathrm{T}} & \mathbf{u}_{i+1}^{\mathrm{T}}\end{pmatrix},\\&\mathbf{u}_i=\begin{pmatrix}\mathbf{u}_{i,1}^{\mathrm{T}} & \cdots & \mathbf{u}_{i,N}^{\mathrm{T}}\end{pmatrix}^{\mathrm{T}}\in\mathbb{R}^{(N\times 3K)\times 1},\\&\mathbf{u}_{i+1,n}=\begin{pmatrix}\boldsymbol{\delta}_{i+1,n,1}^{\mathrm{T}} & \cdots & \boldsymbol{\delta}_{i+1,n,K}^{\mathrm{T}}\end{pmatrix}^{\mathrm{T}}\in\mathbb{R}^{3K\times 1},\end{aligned}\tag{3}$$

where $\mathbf{u}_{i+1}$ is the nodal displacement vector of the group of finite element nodes in the joint $i+1$, and the format of $\mathbf{u}_i$ is similar to that of $\mathbf{u}_{i+1}$. $\mathbf{u}_{i+1,n}$ denotes the nodal displacement vector of the group of finite element nodes in interface n of joint $i+1$ (N interfaces in total), and $\boldsymbol{\delta}_{i+1,n,k}$ is the three-dimensional translational displacement vector of the kth node $N_{i+1,n,k}$ in interface n (K nodes in total) (Figure 4). In this case, joint i is the fixed joint.

Based on the rigid multipoint constraints, $\boldsymbol{\delta}_{i+1,n,k}$ is expressed as follows in terms of a condensation node in the interface n:

$$\boldsymbol{\delta}_{i+1,n,k}=\mathbf{r}_{i+1,n,k}\times\boldsymbol{\varepsilon}_{i+1,n}+\boldsymbol{\delta}_{i+1,n},\tag{4}$$

where $\boldsymbol{\delta}_{i+1,n}$ and $\boldsymbol{\varepsilon}_{i+1,n}$ denote the translational and rotational motions of the condensation node $N_{i+1,n}$, respectively. $\mathbf{r}_{i+1,n,k}$ is the position vector from $N_{i+1,n,k}$ to $N_{i+1,n}$ evaluated in the local frame $\mathcal{K}_{i+1,n}$.

Similarly, assume that the condensation nodes in the joint $i+1$, $N_{i+1,n}$(n=1–N), have a consistent deformation field, then the rigid multipoint constraints can be used at the joint/interface level (Figure 5). The mapping of the nodal displacement vectors between the group of finite element nodes in the joint $i+1$ and a condensation node in the joint $i+1$ is derived as follows from eq. (4):

$$\begin{aligned}&\mathbf{u}_{i+1}=\mathbf{T}_{i+1}\overline{\mathbf{U}}_{i+1},\\&\mathbf{T}_{i+1}=\begin{bmatrix}\mathbf{T}_{i+1,1}{}^{i+1,1}\mathbf{X}_{i+1}\\ \vdots\\ \mathbf{T}_{i+1,N}{}^{i+1,N}\mathbf{X}_{i+1}\end{bmatrix},\mathbf{T}_{i+1,n}=\begin{bmatrix}1_{3\times 3} & \mathbf{r}_{i+1,n,1}\times\\ \vdots & \vdots\\ 1_{3\times 3} & \mathbf{r}_{i+1,n,K}\times\end{bmatrix},\\&{}^{i+1}\mathbf{X}_{i+1,n}=\begin{bmatrix}\mathbf{1}_{3\times 3} & \mathbf{r}_{i+1,n}\times\\ \mathbf{0} & \mathbf{1}_{3\times 3}\end{bmatrix},\end{aligned}\tag{5}$$

where $\overline{\mathbf{U}}_{i+1}=\begin{pmatrix}\boldsymbol{\delta}_{i+1}^{\mathrm{T}} & \boldsymbol{\varepsilon}_{i+1}^{\mathrm{T}}\end{pmatrix}^{\mathrm{T}}$ indicates the nodal displacement vector of the node N_{i+1} created at the center of the joint $i+1$ (Figure 5). $\boldsymbol{\varepsilon}_{i+1}$ and $\boldsymbol{\delta}_{i+1}$ are the displacements along the rotational and translational motions, respectively, of the condensation node N_{i+1} measured in the local frame $\mathcal{K}_{i+1}$. $\mathbf{r}_{i+1,n}$ is the position vector from $N_{i+1,n}$ to N_{i+1}. $\mathbf{r}_*\times$ is the skew-symmetric matrix of $\mathbf{r}_*$ related to its vector product, and $1_{3\times 3}$ denotes the three-order unit matrix. ${}^{i+1}\mathbf{X}_{i+1,n}$ represents the adjoint transformation matrix of the frame $\mathcal{K}_{i+1,n}$ with respect to $\mathcal{K}_{i+1}$, and ${}^{i+1,n}\mathbf{X}_{i+1}$ is the inverse matrix of ${}^{i+1}\mathbf{X}_{i+1,n}$. $\mathbf{T}_{i+1,n}$ represents the reduction matrix from the DOFs of the interface finite element nodes to that of the condensation node in the interface n of the joint $i+1$, and $\mathbf{T}_{i+1}$ denotes the reduction matrix from the DOFs of $\mathbf{u}_{i+1}$ to that of $\overline{\mathbf{U}}_{i+1}$. Similarly, for joint i in the component substructure i, we have $\mathbf{u}_i=\mathbf{T}_i\overline{\mathbf{U}}_i$, where $\mathbf{T}_i$ is the reduction matrix from the DOFs of $\mathbf{u}_i$ to that of $\overline{\mathbf{U}}_i$. Thus, $\mathbf{u}$ in eq. (2) is expressed as

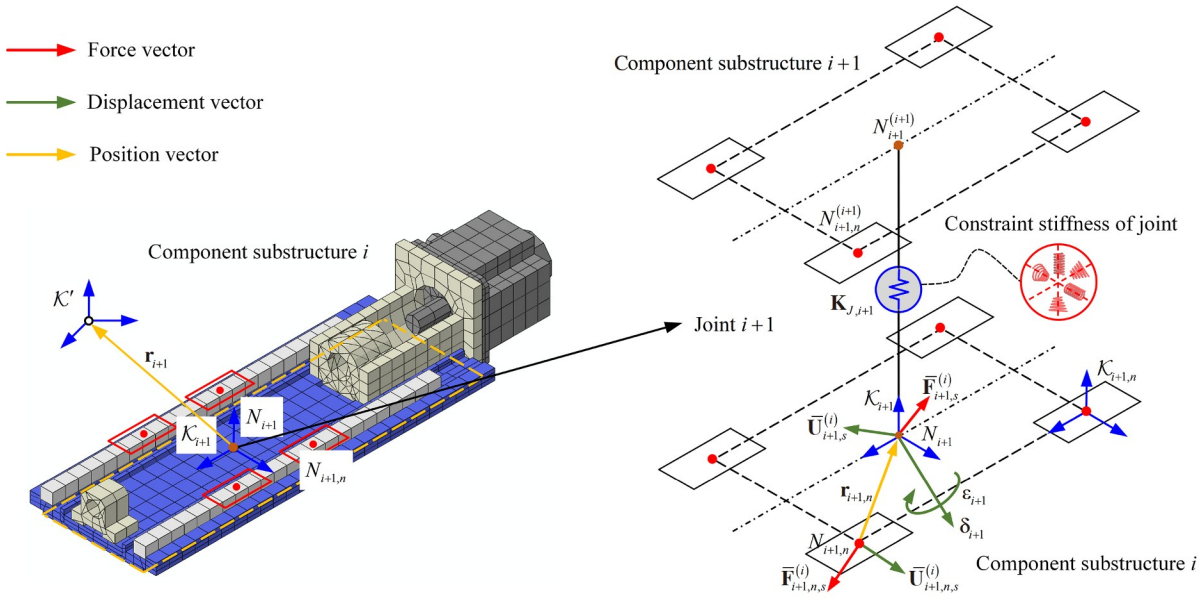

Figure 5 (Color online) Rigid multipoint constraints at joint/interface level.

$$\begin{aligned}&\mathbf{u}=\mathbf{T}\bar{\mathbf{U}},\\&\mathbf{T}=\mathrm{diag}\left[\mathbf{T}_i\ \ \mathbf{T}_{i+1}\ \ 1_{P\times P}\right],\\&\bar{\mathbf{U}}=\left(\mathbf{U}_i^{\mathrm{T}}\ \ \mathbf{U}_{i+1}^{\mathrm{T}}\ \ \mathbf{U}_P^{\mathrm{T}}\right)^{\mathrm{T}},\end{aligned}\tag{6}$$

where $\mathbf{T}$ is the reduction matrix from the CMS method's reduced nodal displacement vector $\mathbf{u}$ to the DOFs of the condensation nodes in the joint i and $i+1$ plus a set of the normalized modal coordinate vector. $1_{P\times P}$ is the P-order unit matrix, and $\bar{\mathbf{U}}_P=\mathbf{u}_P$ denotes the first P-order internal modal coordinates of the component substructure i. The following coordinate transformation is applied to describe the dynamics of each component substructure in the global reference frame $\mathcal{K}'$:

$$\begin{aligned}&\bar{\mathbf{U}}=\mathbf{S}_{i+1}\mathbf{U},\\&\mathbf{S}_{i+1}=\mathrm{diag}\left[\mathbf{R}_{i+1}\ \ \cdots\ \ \mathbf{R}_{i+1}\right],\\&\mathbf{U}=\left(\mathbf{U}_i^{\mathrm{T}}\ \ \mathbf{U}_{i+1}^{\mathrm{T}}\ \ \mathbf{U}_P^{\mathrm{T}}\right)^{\mathrm{T}},\end{aligned}\tag{7}$$

where $\mathbf{R}_{i+1}$ denotes the rotation matrix of $\mathcal{K}_{i+1}$ with respect to $\mathcal{K}'$. $\mathbf{U}_i$, $\mathbf{U}_{i+1}$, and $\mathbf{U}_P$ represent the nodal displacement vectors of nodes N_i, N_{i+1}, and the first P order internal modal coordinates evaluated in the frame $\mathcal{K}'$, respectively. $\mathbf{U}$ denotes the reduced nodal displacement vector of component substructure i measured in the frame $\mathcal{K}'$. We then take into account the number of component substructures and describe them using superscripts. Substituting eq. (7) to eq. (6), and then to eq. (1) leads to

$$\begin{aligned}&\bar{\mathbf{U}}_{i+1,n,s}^{(i)}={}^{i+1,n}\mathbf{X}_{i+1,s}\bar{\mathbf{U}}_{i+1,s}^{(i)},\quad \bar{\mathbf{U}}_{i+1,n,s}^{(i+1)}={}^{i+1,n}\mathbf{X}_{i+1,s}\bar{\mathbf{U}}_{i+1,s}^{(i+1)},\\&\bar{\mathbf{F}}_{i+1,s}^{(i)}=\sum_{n=1}^{N}{}^{i+1,n}\mathbf{X}_{i+1,s}^{\mathrm{T}}\bar{\mathbf{F}}_{i+1,n,s}^{(i)},\quad \bar{\mathbf{F}}_{i+1,n,s}^{(i+1)}=-\bar{\mathbf{F}}_{i+1,n,s}^{(i)},\end{aligned}\tag{8}$$

where $\mathbf{K}^{(i)}$ and $\mathbf{M}^{(i)}$ are the reduced stiffness and mass matrices, respectively. $\mathbf{F}^{(i)}$ denotes the reduced force vector of component substructure i measured in the frame $\mathcal{K}'$.

Based on the constraint interface synthesis method and rigid multipoint constraints at the joint/interface level, the dynamics of each component substructure in the 3-PRS power head are described using two condensation nodes and the first P-order elastic modes, leading to a minimum group of generalized coordinates with $(12+P)$DOFs. Therefore, the dimensions of calculation are significantly reduced than that of FEA.

3.2 Stiffness model of the joint substructures

This section establishes an analytical stiffness model of the joint substructures, including the actuated (P joint) and passive (R and S joints) joints. Taking the actuated prismatic joint $i+1$ as an example, Figure 5 illustrates a schematic diagram of its constraint system. From the rigid multipoint constraint and the virtual work principle, the mapping of the nodal displacement vectors along the constraint motions of the condensation nodes between the interfaces and the joint is formulated as follows:

$$\begin{aligned}&\bar{\mathbf{U}}_{i+1,n,s}^{(i)}={}^{i+1,n}\mathbf{X}_{i+1,s}\bar{\mathbf{U}}_{i+1,s}^{(i)},\\&\bar{\mathbf{U}}_{i+1,n,s}^{(i+1)}={}^{i+1,n}\mathbf{X}_{i+1,s}\bar{\mathbf{U}}_{i+1,s}^{(i+1)},\\&\bar{\mathbf{F}}_{i+1,s}^{(i)}=\sum_{n=1}^{N}{}^{i+1,n}\mathbf{X}_{i+1,s}^{\mathrm{T}}\bar{\mathbf{F}}_{i+1,n,s}^{(i)},\\&\bar{\mathbf{F}}_{i+1,n,s}^{(i+1)}=-\bar{\mathbf{F}}_{i+1,n,s}^{(i)},\end{aligned}\tag{9}$$

where $\bar{\mathbf{U}}_{i+1,n,s}^{(i)}$ and $\bar{\mathbf{U}}_{i+1,n,s}^{(i+1)}$ are the 5×1 nodal displacements

of nodes $N_{i+1,n}^{(i)}$ and $N_{i+1,n}^{(i+1)}$, respectively, along the constraint motions evaluated in the frame $\mathcal{K}_{i+1,n}$ (Figure 5). $\overline{\mathbf{U}}_{i+1,s}^{(i)}$ and $\overline{\mathbf{U}}_{i+1,s}^{(i+1)}$ are the 5×1 nodal displacements of nodes $N_i^{(i)}$ and $N_i^{(i+1)}$, respectively, along the constraint motions evaluated in the frame $\mathcal{K}_{i+1}$. ${}^{i+1,n}\mathbf{X}_{i+1,s}$ is the transformation matrix created by removing the ${}^{i+1,n}\mathbf{X}_{i+1}$ row and column related to the translational motion along the moving axis, thereby providing a 5×5 matrix consistent with the above-reduced 5×1 vectors. $\overline{\mathbf{F}}_{i+1,n,s}^{(i)}$ and $\overline{\mathbf{F}}_{i+1,s}^{(i)}$ are the 5×1 force vectors of nodes $N_{i+1,n}^{(i)}$ and $N_{i+1}^{(i)}$, respectively, along the constraint motions. For interface n in the joint substructure $i+1$, Hooke's law gives

$$\overline{\mathbf{F}}_{i+1,n,s}^{(i)}=\mathbf{K}_{J,i+1,n}\left(\overline{\mathbf{U}}_{i+1,n,s}^{(i+1)}-\overline{\mathbf{U}}_{i+1,n,s}^{(i)}\right), \tag{10}$$

where $\mathbf{K}_{J,i+1,n}$ is a 5×5 contact stiffness matrix of interface n in the joint substructure $i+1$ (Figure 4) that can be generated using the sample handbook. Substituting eq. (10) into eq. (9) leads to

$$\mathbf{K}_{J,i+1,s}=\sum_{n=1}^{N}{}^{i+1,n}\mathbf{X}_{i+1,s}^{\mathrm{T}}\mathbf{K}_{J,i+1,n}{}^{i+1,n}\mathbf{X}_{i+1,s}, \tag{11}$$

where $\mathbf{K}_{J,i+1,s}$ represents the 5×5 equivalent constraint stiffness matrix of the joint substructure $i+1$ evaluated in the frame $\mathcal{K}_{i+1}$. Eq. (11) illustrates that the joint comprising the interfaces is actually a parallel system, and the stiffness matrix of which is the linear superposition of the local stiffness matrix of each interface in the frame $\mathcal{K}_{i+1}$.

For the actuated prismatic joint, i is equal to zero. The stiffness matrix of the actuated joint evaluated in the frame $\mathcal{K}'$, $\mathbf{K}_{J,P}$, is represented as the following tensor transformation:

$$\mathbf{K}_{J,P}=\left(\mathbf{X}_{1,s}\mathbf{K}_{J,1,s}^{-1}\mathbf{X}_{1,s}^{\mathrm{T}}+\mathbf{X}_{1,a}K_{J,1,a}^{-1}\mathbf{X}_{1,a}^{\mathrm{T}}\right)^{-1}, \tag{12}$$

where $\mathbf{X}_1$ is the adjoint transformation matrix of the frame $\mathcal{K}_1$ with respect to $\mathcal{K}'$. $\mathbf{X}_{1,s}$ denotes the transformation matrix by removing the $\mathbf{X}_1$ column related to its translational motion, thereby providing a 6×5 transformation matrix. $\mathbf{X}_{1,a}$ represents the transformation vector related to the translational motion along the moving axis of the $\mathbf{X}_1$ columns, thereby providing a 6×1 vector. $K_{J,1,a}$ denotes the equivalent axial stiffness of the feed drive system evaluated in the frame $\mathcal{K}_1$ [33].

The compliance of the passive spherical joint is the linear superposition of the compliance matrices of the passive revolute joints in the spherical joint. Therefore, the stiffness matrices of the passive revolute and spherical joints evaluated in the frame $\mathcal{K}'$ are represented as follows:

$$\mathbf{K}_{J,R}=\mathbf{X}_{2,s}^{-\mathrm{T}}\mathbf{K}_{J,2,s}\mathbf{X}_{2,s}^{-1}, \tag{13}$$

$$\mathbf{K}_{J,S}=\left(\sum_{j=3}^{5}\mathbf{X}_{j,s}\mathbf{K}_{J,j,s}^{-1}\mathbf{X}_{j,s}^{\mathrm{T}}\right)^{-1}, \tag{14}$$

where $\mathbf{K}_{J,j,s}$ denotes the equivalent constraint stiffness matrix of each revolute joint in the spherical joint. The formats and meanings of the transformation and stiffness matrices in eqs. (13) and (14) are similar to those in eq. (12).

3.3 Synthesis model of the 3-PRS power head

This section derives the dynamic model of the 3-PRS power head by assembling all the components and joint substructures. Without considering the smaller inertia of the shafts in the spherical joints, the entire mechanism can be broken down into five-component substructures consisting of a base, three limbs, and a moving platform numbered from 0 to 4 (Figure 6). The ith PRS limb substructure is decomposed into three-component substructures with a connecting board, a slider, and a connecting rod numbered from $1,i$ to $3,i$. A number of nodes $N_b^{(a)}$ and nodal displacement vectors $\mathbf{U}_b^{(a)}$ are set to conveniently synthesize the entire mechanism. a and b denote the component substructure number and the node number in them, respectively. The adjacent nodes are connected through the joint substructure stiffness, ensuring compatibility between the component substructures. The kinetic T and elastic potential V energies of the 3-PRS power head are estimated as follows:

$$\begin{aligned}
&T=T_0+\sum_{i=1}^{3}\sum_{j=1}^{3}T_{j,i}+T_4,\\
&V=V_0+\sum_{i=1}^{3}\sum_{j=1}^{3}V_{j,i}+V_4+\sum_{i=1}^{3}\sum_{k=P,R,S}V_{k,i},\\
&T_m=\frac{1}{2}\left(\dot{\mathbf{U}}^{(m)}\right)^{\mathrm{T}}\mathbf{M}^{(m)}\dot{\mathbf{U}}^{(m)},\\
&V_m=\frac{1}{2}\left(\mathbf{U}^{(m)}\right)^{\mathrm{T}}\mathbf{K}^{(m)}\mathbf{U}^{(m)},\\
&V_{k,i}=\frac{1}{2}\begin{pmatrix}\mathbf{U}_b^{(a)}\\ \mathbf{U}_d^{(c)}\end{pmatrix}^{\mathrm{T}}\begin{bmatrix}\mathbf{K}_{J,k} & -\mathbf{K}_{J,k}\\ -\mathbf{K}_{J,k} & \mathbf{K}_{J,k}\end{bmatrix}\begin{pmatrix}\mathbf{U}_b^{(a)}\\ \mathbf{U}_d^{(c)}\end{pmatrix},\\
&\mathbf{U}^{(m)}=\begin{pmatrix}\mathbf{U}_1^{(m)} & \cdots & \mathbf{U}_n^{(m)} & \mathbf{U}_P^{(m)}\end{pmatrix}^{\mathrm{T}},\\
&m=0,\cdots,(j,i),\cdots,4,i,j=1-3,k=P,R,S,
\end{aligned} \tag{15}$$

where T_m and V_m represent the kinetic and elastic potential energies, respectively, of the component substructure m. $\mathbf{U}^{(m)}$ and $\mathbf{U}_P^{(m)}$ are the nodal displacement vectors of the component substructure m and its internal modal coordinates, respectively. n represents the number of external condensation nodes in the component substructure m. $V_{k,i}$ is the elastic

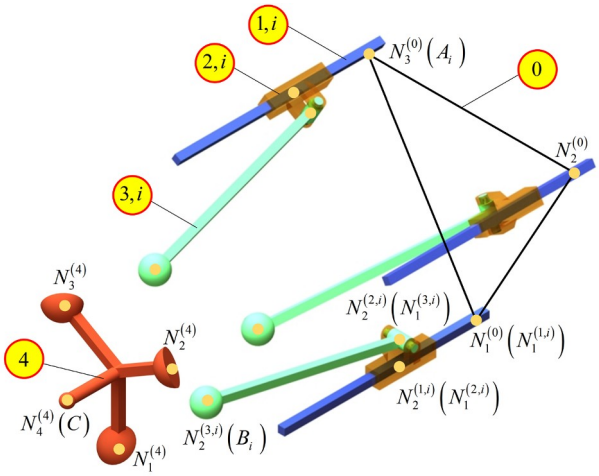

Figure 6 (Color online) Overview of substructure synthesis of the 3-PRS power head.

potential energy of the kth joint substructure in limb i. $\mathbf{U}_b^{(a)}$ and $\mathbf{U}_d^{(c)}$ are the nodal displacement vectors of the nodes connecting the kth joint substructure. The compatibility between $\mathbf{U}_2^{(1,i)}$ and $\mathbf{U}_1^{(2,i)}$ is ensured by $\mathbf{K}_{J,P}$.

Using Lagrange's equation of eq. (15), the entire mechanism's undamped equation of motion is represented in the global reference frame $\mathcal{K}'$ by the following partitioned model.

$$\begin{aligned}&\mathbf{M}\ddot{\mathbf{U}}+\mathbf{K}\mathbf{U}=\mathbf{F},\\&\mathbf{M}=\begin{bmatrix}\mathbf{M}_{\lambda\lambda} & \mathbf{M}_{\lambda q} & \mathbf{M}_{\lambda\eta}\\ & \mathbf{M}_{qq} & \mathbf{M}_{q\eta}\\ \text{sym} & & \mathbf{M}_{\eta\eta}\end{bmatrix},\mathbf{K}=\begin{bmatrix}\mathbf{K}_{\lambda\lambda} & \mathbf{K}_{\lambda q} & \mathbf{K}_{\lambda\eta}\\ & \mathbf{K}_{qq} & \mathbf{K}_{q\eta}\\ \text{sym} & & \mathbf{K}_{\eta\eta}\end{bmatrix},\\&\mathbf{U}=\begin{pmatrix}\boldsymbol{\lambda}\\ \mathbf{q}\\ \boldsymbol{\eta}\end{pmatrix},\mathbf{F}=\begin{pmatrix}\mathbf{F}_C\\ 0\\ 0\end{pmatrix}.\end{aligned}\tag{16}$$

where $\boldsymbol{\lambda}=\mathbf{U}_C\in\mathbb{R}^{6\times1}$ and $\mathbf{F}_C\in\mathbb{R}^{6\times1}$ represent the nodal displacement and force vectors, respectively, of the end-reference point C. $\mathbf{q}\in\mathbb{R}^{144\times1}$ represents the collection of the nodal displacement vectors of all the external condensation nodes in the entire mechanism, except point C. $\boldsymbol{\eta}\in\mathbb{R}^{11P\times1}$ is the collection of the internal modal coordinates of all component substructures. The lower-order dynamics of the holistic mechanism are described using a group of generalized coordinates with $(150+11P)$DOFs.

3.4 Dynamic analysis of the 3-PRS power head

Assume that the dynamic system of the entire mechanism is viscous proportional damping. If the damping distribution of the system of the abovementioned DOFs is denoted as matrix $\mathbf{C}$, then the equation of motion of the entire system in the time domain is given as

$$\mathbf{M}\ddot{\mathbf{U}}(t)+\mathbf{C}\dot{\mathbf{U}}(t)+\mathbf{K}\mathbf{U}(t)=\mathbf{F}(t).\tag{17}$$

Subsequently, substituting $\mathbf{U}(t)=\mathbf{U}(\omega)\mathrm{e}^{\mathrm{j}\omega t}$ into eq. (17) leads to the following frequency response functions (FRFs) of the holistic mechanism in the frequency domain:

$$\begin{aligned}&\mathbf{U}(\omega)=\mathbf{H}(\omega)\mathbf{F}(\omega),\\&\mathbf{H}(\omega)=(\mathbf{K}-\omega^2\mathbf{M}+\mathrm{j}\omega\mathbf{C})^{-1}=\sum_{k=1}^{\infty}\frac{\phi_k\phi_k^{\mathrm{T}}}{k_k-\omega^2m_k+\mathrm{j}\omega c_k},\end{aligned}\tag{18}$$

where m_k, k_k, and c_k are the normalized modal mass, stiffness, and damping of the kth mode shape, respectively. ϕ_k is the normalized reduced nodal displacement vector of the holistic mechanism. For convenience, $\mathbf{U}(\omega)$ and $\mathbf{F}(\omega)$ are denoted as $\mathbf{U}$ and $\mathbf{F}$, respectively. During the machining process, the end-reference point C is excited by the dynamic cutting load $\mathbf{F}_C$. Based on the modal analysis theory, the FRFs of point C are expressed as

$$\begin{aligned}&\mathbf{U}_C=\mathbf{H}_C(\omega)\mathbf{F}_C,\\&\mathbf{H}_C(\omega)=\sum_{k=1}^{\infty}\frac{\phi_{C,k}\phi_{C,k}^{\mathrm{T}}}{k_k-\omega^2m_k+\mathrm{j}\omega c_k},\end{aligned}\tag{19}$$

where $\phi_{C,k}$ is the nodal displacement of point C of the kth mode shape measured in the frame $\mathcal{K}'$. Considering the excitations along the u, v, and w directions, the FRFs of point C along the $i(i=u,v,w)$ direction are represented as

$$\begin{aligned}&U_{C,i}=H_{C,ii}(\omega)F_{C,i},\\&H_{C,ii}(\omega)=\sum_{k=1}^{m}\frac{(f_{C,i})_k}{1-(\omega/\omega_k)^2+2\xi_k(\omega/\omega_k)\mathrm{j}},\\&(f_{C,i})_k=\frac{\phi_{C_i,k}^2}{k_k},\end{aligned}\tag{20}$$

where $U_{C,i}$ denotes the nodal displacement of point C along the ith direction, and $F_{C,i}$ is the excitation force of point C along the ith direction. $\phi_{C_i,k}$ represents the nodal displacement of point C in the k-order mode shape along the ith direction. ξ_k and ω_k represent the damping ratio and natural frequency of the k-order mode, respectively. $H_{C,ii}(\omega)$ is the ith main diagonal element of $\mathbf{H}_C(\omega)$. $(f_{C,i})_k$ denotes the kth modal flexibility of point C. When the exciting frequency ω is zero, then we have

$$C_i=H_{C,ii}(0)=\sum_{k=1}^{\infty}(f_{C,i})_k,\tag{21}$$

where C_i represents the static compliance of point C along the ith direction, and $(f_{C,i})_r/C_i$ is the ratio of the rth modal flexibility and the static compliance illustrating the contribution of the rth modal flexibility to the static compliance

along the *i*th direction.

We define the following energy distribution indices to evaluate the energy contribution of each substructure to the entire dynamic system:

$$\gamma_{r,i}=\frac{T_{r,i}}{T_r},\left(f_{C,i}\right)_k=\frac{\phi_{C_i,k}^2}{k_k}, \tag{22}$$

where $\gamma_{r,i}$ and $\mu_{r,i}$ denote the distribution rates of the kinetic and elastic potential energies, respectively, of the component or joint substructure i in the rth order mode.

4 Numerical example

In this section, one type of 3-PRS power head is taken as an illustration to demonstrate the accuracy and efficiency of the presented dynamic modeling and analysis approach. Figure 7 shows the task workspace of the 3-PRS mechanism (curved triangular prism with h height) defined by the nutation and precession angles and the stroke along the z direction (θ=0°–30°, ψ=0°–360°, and s=0–h mm). Table 1 gives the geometric dimensional and task workspace parameters of the mechanism. A reference configuration is defined when $q_1=q_2=q_3=(q_{\min}+q_{\max})/2$, where $q_{\min}$ and $q_{\max}$ denote the minimum and maximum strokes, respectively, of the screw-nut system in the PRS limb.

Table 2 shows the structural parameters of each elastic interface and the compliance matrices in the actuated prismatic and passive revolute and spherical joints evaluated in the corresponding local reference frames. For convenience, the order of the internal elastic modes P for each component substructure in eq. (2) is identically set to 3, resulting in 15×15 reduction mass and stiffness matrices. These data were obtained from the Super-element Creation module of the SAMCEF commercial FEA software. Consequently, the DOFs of the proposed semi-analytical dynamic model are 183.

Figures 8 and 9 illustrate the lower-order mode shapes of the 3-PRS mechanism obtained from the FEA model and predicted by the proposed semi-analytical model at the reference configuration, respectively. The FE software's corresponding boundary conditions, material properties, and contact stiffnesses are set consistent with those parameters of the developed model, resulting in an FE model with 3.05×10^5 DOFs. The 1st and 2nd mode shapes are primarily the translational vibrations along the u and v directions of the moving platform, respectively. The 3rd mode shape is primarily the torsional vibration about the w direction of the moving platform, and the 4th is the combination of the torsional vibration of the moving platform and the translational vibration of limbs 2 and 3. The 5th mode shape is the translational vibrations of sliders in three parallel limbs along the direction of motion. The 6th and 7th mode shapes

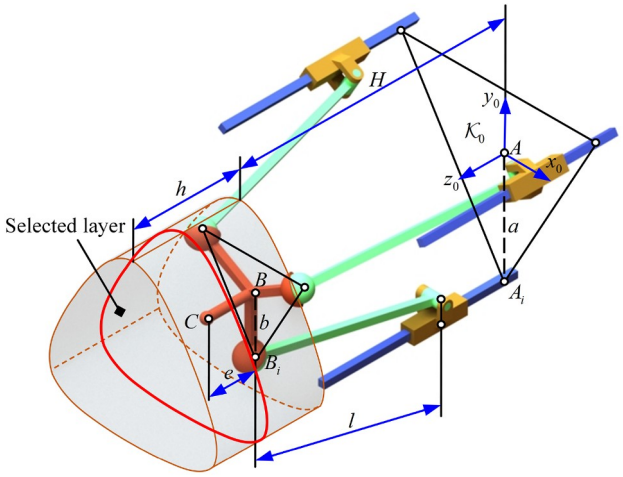

Figure 7 (Color online) Task workspace of the 3-PRS power head.

Table 1 Geometrical parameters of the 3-PRS parallel mechanism (mm)

Parameters	Value
a	330
b	165
l	350
e	315
H	1175
h	200

are the translational vibrations of sliders in limbs 1 and 2 along the direction of motion, respectively. The 8th mode shape is the bending vibration of the connecting rods in limbs 1 and 3. The dynamic responses of the end-reference point in the 3rd, 4th, and 8th orders are essentially zero. Obviously, the lower-order mode shapes estimated by the developed model agree very well with those from FEA. The modal assurance criterion (MAC) is employed further to verify the above two models' consistency as

$$\mathrm{MAC}_{ij}=\frac{\left(\boldsymbol{\Phi}_{\mathrm{FE},i}^{\mathrm{T}}\boldsymbol{\Phi}_{\mathrm{RS},j}\right)^2}{\left(\boldsymbol{\Phi}_{\mathrm{FE},i}^{\mathrm{T}}\boldsymbol{\Phi}_{\mathrm{FE},i}\right)\left(\boldsymbol{\Phi}_{\mathrm{RS},j}^{\mathrm{T}}\boldsymbol{\Phi}_{\mathrm{RS},j}\right)},i,j=1,2,\cdots,8, \tag{23}$$

where $\boldsymbol{\Phi}_{\mathrm{FE},i}$ and $\boldsymbol{\Phi}_{\mathrm{RS},j}$ are the ith and jth mode shapes of the FE and the developed reduced semi-analytical model, respectively. Figure 10 shows the MAC of the first eight-order mode shapes between the two models, and it is evident that the diagonal elements' values are much higher than the rest non-diagonal elements' values (0.92 against 0.25), demonstrating the accuracy of the developed model for predicting the lower-order mode shapes.

Figure 11 illustrates the FRFs of the end-reference point along the u, v, and w axes of K' predicted by the proposed model and obtained from FEA at the reference configuration, respectively. The damping ratios for the first eight-order

Table 2 Local reference frames and compliance matrices of elastic interfaces in the 3-PRS parallel mechanism (i=1,2,3)[a)]

M	$\mathcal{K}_m$, $\mathcal{K}_{m,n}$	$\mathbf{K}_{J,m,n}^{-1}$ (unit: N, m, rad)
1,i	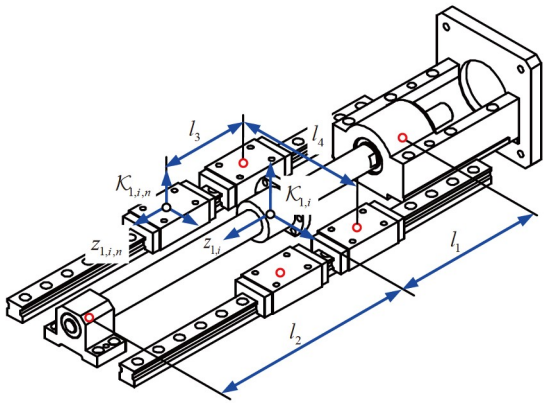	$l_1 = 0.15 + q_i,\ l_2 = 0.40 - q_i$ $l_3 = 0.160,\ l_4 = 0.215$ $K_{J,1,a}^{-1} = \left(\left(k_{b1}^{-1} + k_{l1}^{-1}\right)^{-1} + \left(k_{b2}^{-1} + k_{l2}^{-1}\right)^{-1}\right)^{-1} + k_{nut}^{-1}$ $k_{l1}^{-1} = l_1 / EA,\ k_{l2}^{-1} = l_2 / EA,\ EA = 2.138 \times 10^8$ $k_{b1}^{-1} = 5 \times 10^{-9},\ k_{b2}^{-1} = 4 \times 10^{-9},\ k_{nut}^{-1} = 1.60 \times 10^{-9}$ $\mathbf{K}_{J,1,i,n}^{-1} = \begin{bmatrix} 1.87 & & & & & \\ & 0.98 & & & & \\ & & 1.87 \times 10^3 & & & \\ & & & 1.87 \times 10^3 & & \\ & & & & 4.00 \times 10^3 & \end{bmatrix} \times 10^{-9}$ $n = 1, 2, 3, 4$
2,i	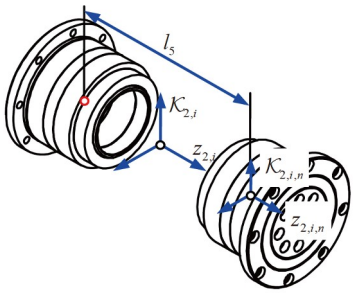	$l_5 = 0.197$ $\mathbf{K}_{J,2,i,n}^{-1} = \begin{bmatrix} 0.43 & & & & & \\ & 0.43 & & & & \\ & & 1.16 & & & \\ & & & 0.83 \times 10^3 & & \\ & & & & 0.83 \times 10^3 & \end{bmatrix} \times 10^{-9}$ $n = 1, 2$
3,i 4,i 5,i	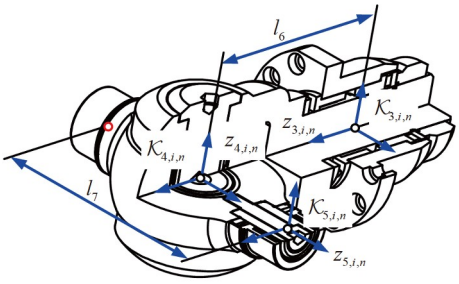	$l_6 = 0.105,\ l_7 = 0.132$ $\mathbf{K}_{J,3,i,n}^{-1} = \begin{bmatrix} 0.93 & & & & & \\ & 0.93 & & & & \\ & & 0.68 & & & \\ & & & 6.10 \times 10^3 & & \\ & & & & 6.10 \times 10^3 & \end{bmatrix} \times 10^{-9}$ $\mathbf{K}_{J,4,i,n}^{-1} = \begin{bmatrix} 3.70 & & & & & \\ & 3.70 & & & & \\ & & 14.29 & & & \\ & & & 1.00 \times 10^3 & & \\ & & & & 1.00 \times 10^3 & \end{bmatrix} \times 10^{-9}$ $\mathbf{K}_{J,5,i,n}^{-1} = \begin{bmatrix} 3.70 & & & & & \\ & 3.70 & & & & \\ & & 2.70 & & & \\ & & & 1.00 \times 10^3 & & \\ & & & & 1.00 \times 10^3 & \end{bmatrix} \times 10^{-9}$ $n = 1, 2$

a) k_{nut}, k_{b1}, k_{b2} are compression or extension stiffness coefficients of the nut, front and rear support bearings, respectively. EA is the tensile modulus of the lead-screw. q_i denotes the stroke of the screw-nut system in the ith PRS limb.

modes are set at 0.025 identically in the two models mentioned above. Obviously, the proposed model's FRFs agree well with those obtained by the FEA. The discrepancy of natural frequencies between the above two models is less than 8.16%, as shown in Table 3, demonstrating the accuracy of the developed model for predicting lower-order natural frequencies. From Figure 11 and Table 3, the lower-order natural frequencies predicted using the proposed model are slightly higher than those obtained using the FEA model. In the meantime, the dynamic response of each lower-order mode has the opposite tendency. This phenomenon can primarily be attributed to the fact that: (1) the rigid multipoint constraint increases the rigidity of the interface and joint, leading to an over-estimation of elastic potential energy in the proposed semi-analytical model; (2) neglecting the inertia of shafts in spherical joints results in the under-esti-

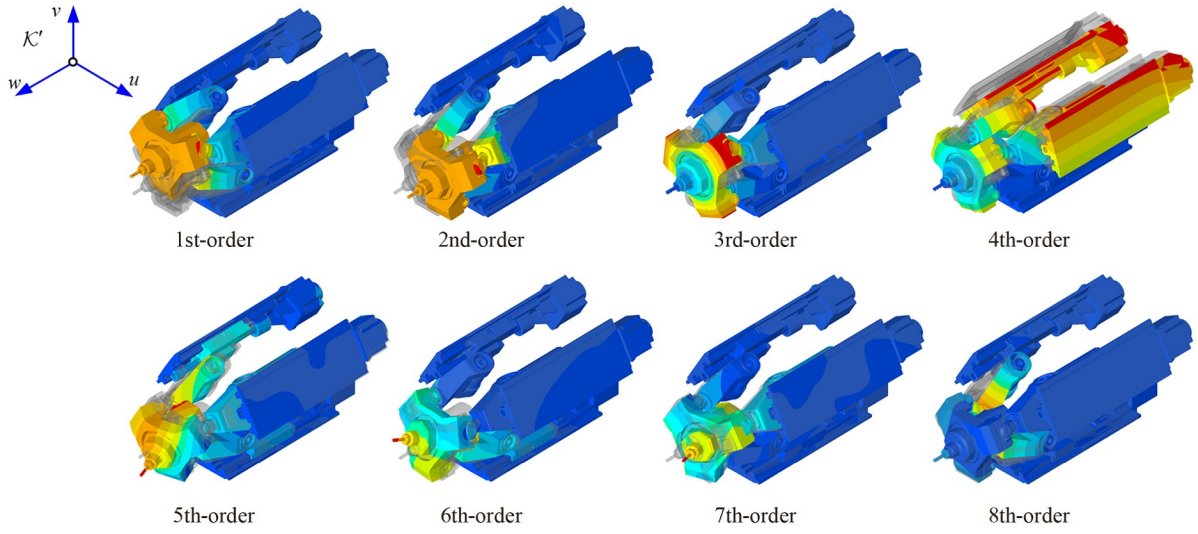

Figure 8 (Color online) The lower-order mode shapes obtained from the FEA.

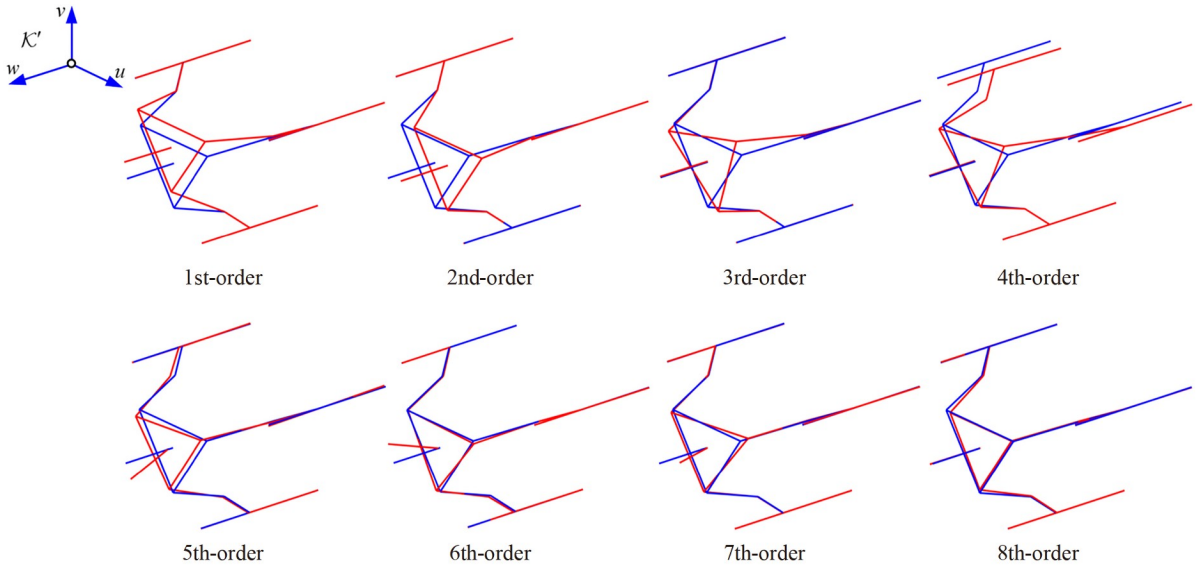

Figure 9 (Color online) The lower-order mode shapes predicted by the developed model.

mation of the kinetic energy of the mechanical system.

In Figure 12, a further demonstration of the accuracy of the developed model under more general nutation and precession angles is provided by selecting nine additional configurations in the reference layer (θ=0°–30°, ψ=0°–360°, z=1275 mm) of the task workspace. This is performed by considering the central symmetry of the 3-PRS mechanism in the task workspace. Table 4 presents the values of the nutation and precession angles for each selected configuration in the reference layer. Figure 13 illustrates the discrepancy of the first eight-order natural frequencies between the proposed dynamic model and the FEA under each selected configuration. The root mean square (RMS) value of the first eight-order natural frequencies is employed to evaluate the discrepancy of each selected configuration (Table 4). The RMS discrepancy of the lower-order natural frequencies between the developed model and the FEA is less than 5.92%, demonstrating the accuracy of the proposed model in the entire task workspace.

With these persuasive results, the first six-order natural frequency distributions over the reference layer of the task workspace are predicted using the proposed dynamic model (Figure 14). The prediction results were processed using an i7-8750 CPU and 16 GB RAM laptop. The overall calculation time for solving 3600×100 configurations was less than 20 s. In contrast, obtaining the dynamics for a single configuration in the FEA model required at least 150 s, demonstrating the efficiency of the developed model for

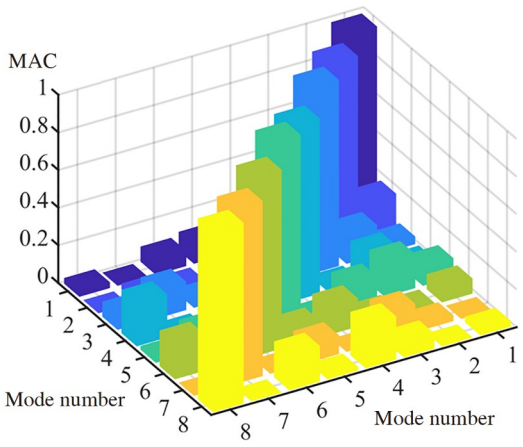

Figure10 (Color online) MAC of lower-order mode shapes between the proposed model and FEA.

predicting lower-order natural frequencies over the task workspace.

Figure 15 shows the contributions of the modal flexibility of the lower-order modes to the static compliance of the end-reference point along the u, v, and w directions at the reference configuration. It is obvious that the 2nd, 1st, and 5th order modes have considerable impacts on the static compliances of the end-reference point along the u, v, and w directions, respectively (i.e., $\left(f_{C,u}\right)_2 / C_u = 72.95\%$, $\left(f_{C,v}\right)_1 / C_v = 75.45\%$, and $\left(f_{C,w}\right)_5 / C_w = 76.29\%$). A higher contribution of the modal flexibility represents that the configuration between the modal stiffness and mass in the corresponding mode is suboptimal, resulting in a prominent week mode. The optimization design needs to be conducted aiming at these weak modes. In this case, the 2nd, 1st, and 5th order modes are determined as the prominent week modes. Figures 16 and 17 give the distributions of kinetic and elastic potential energies of component and joint substructures in the 1st and 2nd order prominent week modes at the reference configuration, respectively. It is evident that the kinetic energies of the 1st and 2nd order modes are primarily distributed on the moving platform, and the connecting rods in three limbs have relatively significant contributions to the 1st and 2nd orders' kinetic energies. The elastic potential energies of the 1st and 2nd order modes are primarily distributed on the moving platform, connecting rods, and spherical joints in three limbs. Component or joint substructures with higher kinetic energy distribution tend to have higher mass or lower stiffness than others, whereas substructures with higher elastic potential energy distribution tend to have lower stiffness. Therefore, the following optimization strategies are proposed: (1) Adopting the lightweight design for the moving platform while ensuring its stiffness requirements; (2) improving the stiffness of connecting roes in three limbs by changing the stiffener topology; (3) selecting the supporting bearings in the spherical joints with higher stiffnesses.

Table 3 Lower-order natural frequencies calculated by the developed model and the FEA at the reference configuration

Mode number	Semi-analytical (Hz)	FEA (Hz)	Discrepancy (%)
1st	57.84	56.5	2.37
2nd	59.56	57.89	2.88
3rd	142.99	138.89	2.95
4th	155.84	150.54	3.52
5th	215.65	202.53	6.48
6th	226.93	214.88	5.61
7th	238.68	223.13	6.97
8th	274.22	253.53	8.16

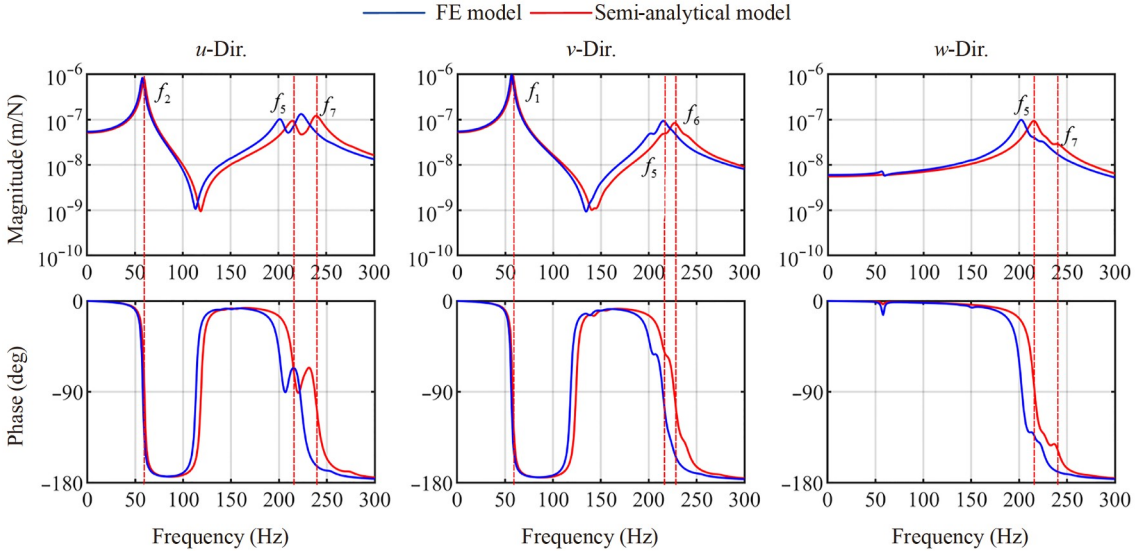

Figure 11 (Color online) FRF comparisons between the proposed and the FEA models at the reference configuration.

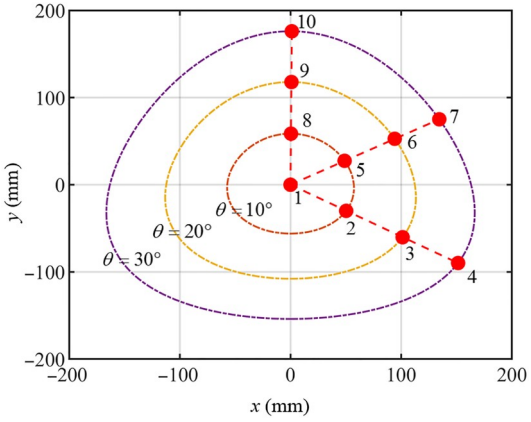

Figure 12 (Color online) Selected configurations in the reference layer.

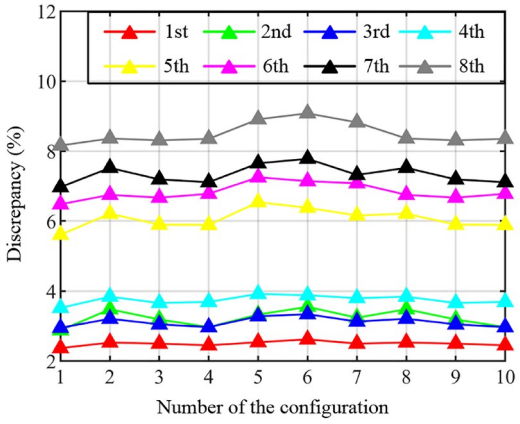

Figure 13 (Color online) Discrepancy of lower-order natural frequencies between the proposed model and FEA at each selected configuration.

Table 4 Nutation and precession angles and RMS discrepancy in the lower-order natural frequencies at each selected configuration in the reference layer

Configuration number	θ	ψ	RMS discrepancy (%)
1	0°	0°	5.29
2	10°	60°	5.64
3	20°	60°	5.47
4	30°	60°	5.46
5	10°	120°	5.88
6	20°	120°	5.92
7	30°	120°	5.71
8	10°	180°	5.64
9	20°	180°	5.47
10	30°	180°	5.46

5 Conclusions

This study introduces an efficient approach for the accurate dynamic modeling and analysis of a 3-PRS power head. The following conclusions are derived from this work.

(1) By employing the rigid multipoint constraints at the joint/interface level, an improved reduced dynamic model of the component substructures in the 3-PRS power head is formulated using a minimum set of generalized coordinates for external nodes. A compact explicit expression for the stiffness model of the joint substructure is then described through the screw theory, leading to the mapping between the local interface constraint and global stiffness. Finally, the total kinetic and elastic potential energies of the holistic power head are formulated, and the dynamic model is de-

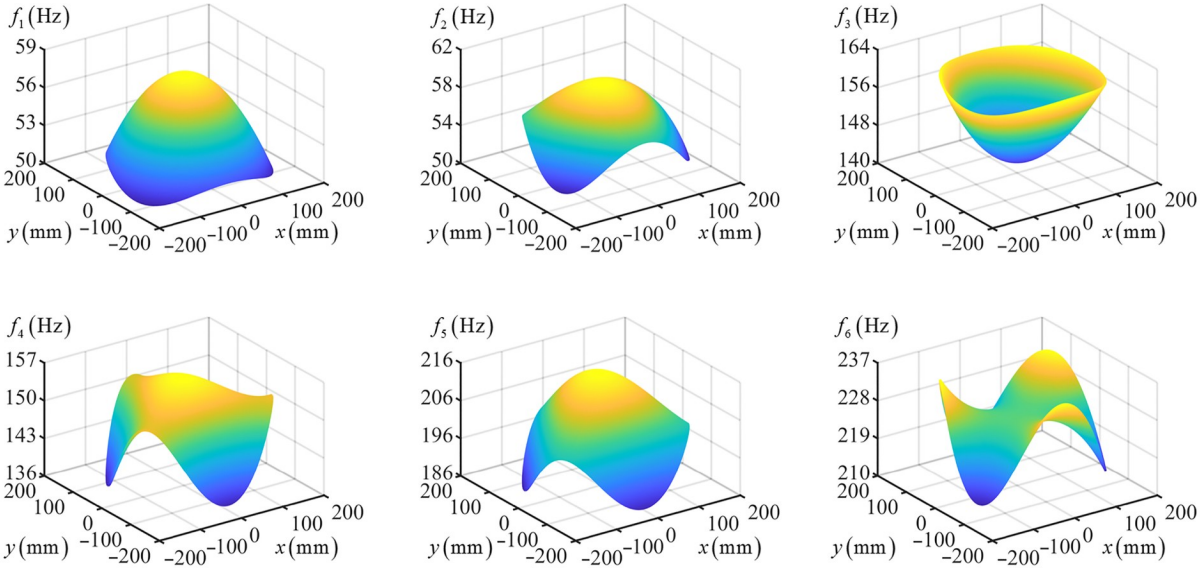

Figure 14 (Color online) Natural frequency distributions of the 3-PRS power head over the reference layer.

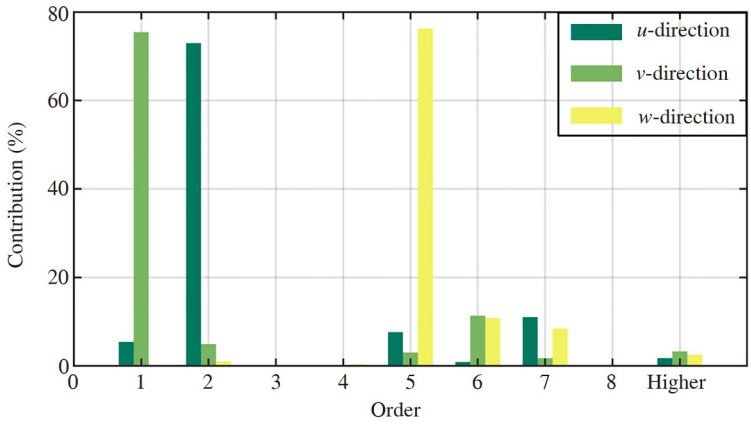

Figure 15 (Color online) Contributions of the rth modal flexibility to the static compliance of the end-reference point.

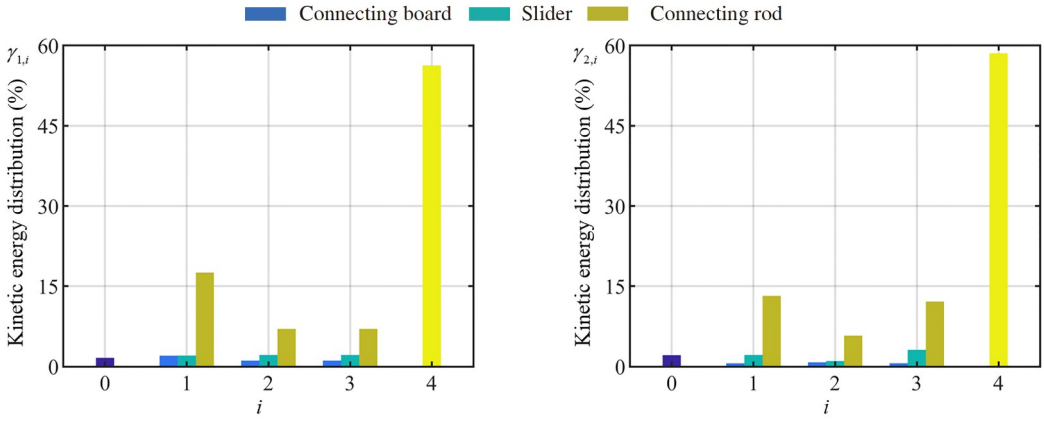

Figure 16 (Color online) Distributions of the kinetic energy of the 1st and 2nd order modes. i=0: base, i=1, 2, 3: limbs 1 to 3, i=4: moving platform.

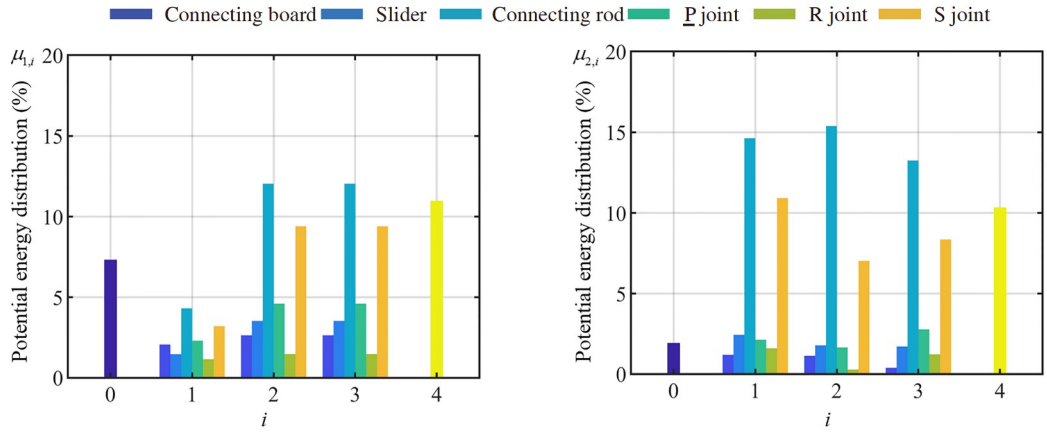

Figure 17 (Color online) Distributions of the elastic potential energy of the 1st and 2nd order modes. i=0: base, i=1, 2, 3: limbs 1 to 3, i=4: moving platform.

rived from the Lagrange equation.

(2) Taking one type of a 3-PRS power head for demonstration, the accuracy and effectiveness of the developed approach are illustrated by comparative studies of lower-order mode shapes, natural frequencies, and FRFs against those of an FEA model. The results indicated that the lower-order natural frequency distributions over the reference layer in the task workspace can be predicted with a considerable

reduction in computational time. The optimization strategies are presented based on modal flexibility and energy distribution analyses, which are extremely useful for the optimization design under the virtual machine framework. This method is systematic and general enough to be applied to the dynamic modeling and analysis of other PKMs.

This work was supported by the EU Horizon 2020 research and innovation program under the Marie Skłodowska-Curie (Grant No. 734272) and the China Scholarship Council (Grant No. 201908060118).

1 Wu J, Wang J, Wang L, et al. Dynamics and control of a planar 3-DOF parallel manipulator with actuation redundancy. Mech Mach Theory, 2009, 44: 835–849
2 Dong C, Liu H, Huang T, et al. A screw theory-based semi-analytical approach for elastodynamics of the tricept robot. J Mech Robotics, 2019, 11: 1
3 Wu J, Ye H, Yu G, et al. A novel dynamic evaluation method and its application to a 4-DOF parallel manipulator. Mech Mach Theory, 2022, 168: 104627
4 Li Y G, Liu H T, Zhao X M, et al. Design of a 3-DOF PKM module for large structural component machining. Mech Mach Theory, 2010, 45: 941–954
5 Wu J, Yu G, Gao Y, et al. Mechatronics modeling and vibration analysis of a 2-DOF parallel manipulator in a 5-DOF hybrid machine tool. Mech Mach Theory, 2018, 121: 430–445
6 Dong C, Liu H, Xiao J, et al. Dynamic modeling and design of a 5-DOF hybrid robot for machining. Mech Mach Theory, 2021, 165: 104438
7 Tyapin I, Hovland G. The Gantry-Tau parallel kinematic machine—Kinematic and elastodynamic design optimisation. Meccanica, 2011, 46: 113–129
8 Portman V T, Chapsky V S, Shneor Y. Evaluation and optimization of dynamic stiffness values of the PKMs: Collinear stiffness value approach. Mech Mach Theory, 2014, 74: 216–244
9 Gherman B, Pisla D, Vaida C, et al. Development of inverse dynamic model for a surgical hybrid parallel robot with equivalent lumped masses. Rob Comput Integr Manuf, 2012, 28: 402–415
10 Zhao Y, Gao F, Dong X, et al. Dynamics analysis and characteristics of the 8-PSS flexible redundant parallel manipulator. Rob Comput Integr Manuf, 2011, 27: 918–928
11 Zhang J, Zhao Y, Jin Y. Kinetostatic-model-based stiffness analysis of Exechon PKM. Rob Comput Integr Manuf, 2016, 37: 208–220
12 Cammarata A, Caliò I, DUrso D, et al. Dynamic stiffness model of spherical parallel robots. J Sound Vib, 2016, 384: 312–324
13 Lian B, Wang L, Wang X V. Elastodynamic modeling and parameter sensitivity analysis of a parallel manipulator with articulated traveling plate. Int J Adv Manuf Technol, 2019, 102: 1583–1599
14 Son H, Choi H J, Park H W. Design and dynamic analysis of an archtype desktop reconfigurable machine. Int J Mach Tools Manuf, 2010, 50: 575–584
15 Ma Y, Niu W, Luo Z, et al. Static and dynamic performance evaluation of a 3-DOF spindle head using CAD-CAE integration methodology. Rob Comput Integr Manuf, 2016, 41: 1–12
16 Ma Y, Liu H, Zhang M, et al. Elasto-dynamic performance evaluation of a 6-DOF hybrid polishing robot based on kinematic modeling and CAE technology. Mech Mach Theory, 2022, 176: 104983
17 Rui X, He B, Lu Y, et al. Discrete time transfer matrix method for multibody system dynamics. Multibody Syst Dyn, 2005, 14: 317–344
18 Rui X, Wang G, Lu Y, et al. Transfer matrix method for linear multibody system. Multibody Syst Dyn, 2008, 19: 179–207
19 Rui X, Bestle D, Zhang J, et al. A new version of transfer matrix method for multibody systems. Multibody Syst Dyn, 2016, 38: 137–156
20 Chen G, Rui X, Abbas L K, et al. A novel method for the dynamic modeling of Stewart parallel mechanism. Mech Mach Theory, 2018, 126: 397–412
21 Chen G, Rui X, Gu J, et al. Development of an object-oriented framework for the vibration characteristic computation of multibody systems. Adv Eng Software, 2020, 148: 102874
22 Law M, Altintas Y, Srikantha Phani A. Rapid evaluation and optimization of machine tools with position-dependent stability. Int J Mach Tools Manuf, 2013, 68: 81–90
23 Law M, Ihlenfeldt S, Wabner M, et al. Position-dependent dynamics and stability of serial-parallel kinematic machines. CIRP Ann, 2013, 62: 375–378
24 Liang D, Song Y, Sun T, et al. Rigid-flexible coupling dynamic modeling and investigation of a redundantly actuated parallel manipulator with multiple actuation modes. J Sound Vib, 2017, 403: 129–151
25 Wu L, Wang G, Liu H, et al. An approach for elastodynamic modeling of hybrid robots based on substructure synthesis technique. Mech Mach Theory, 2018, 123: 124–136
26 Wu L, Dong C, Wang G, et al. An approach to predict lower-order dynamic behaviors of a 5-DOF hybrid robot using a minimum set of generalized coordinates. Rob Comput Integr Manuf, 2021, 67: 102024
27 Heirman G H K, Desmet W. Interface reduction of flexible bodies for efficient modeling of body flexibility in multibody dynamics. Multibody Syst Dyn, 2010, 24: 219–234
28 Ni Y, Lu C, Zhou H, et al. A spatial grid point compensation method for a one-translational two-rotational power head. Proc Inst Mech Engineers Part C-J Mech Eng Sci, 2022, 236: 8348–8357
29 Ma Y, Tian Y, Song Y. A screw theory-based approach for conservative stiffness mapping of 3-PRS parallel mechanism. In: Proceedings of the 4th WRC Symposium on Advanced Robotics and Automation (WRC SARA). Beijing, 2022. 19–24
30 Craig R R, Bampton M C C. Coupling of substructures for dynamic analyses. AIAA J, 1968, 6: 1313–1319
31 Paz M. Dynamic condensation. AIAA J, 1984, 22: 724–727
32 Masson G, Ait Brik B, Cogan S, et al. Component mode synthesis (CMS) based on an enriched ritz approach for efficient structural optimization. J Sound Vib, 2006, 296: 845–860
33 Altintas Y, Verl A, Brecher C, et al. Machine tool feed drives. CIRP Ann, 2011, 60: 779–796